ELSEVIER

Contents lists available at ScienceDirect

Journal of Fluids and Structures

journal homepage: www.elsevier.com/locate/ifs



Propulsive performance and vortex wakes of multiple tandem foils pitching in-line



Pan Han^a, Yu Pan^a, Geng Liu^b, Haibo Dong^{a,*}

- a Department of Mechanical & Aerospace Engineering, University of Virginia, Charlottesville, VA 22904, United States of America
- ^b Department of Engineering, King's College, Wilkes-Barre, PA 18711, United States of America

ARTICLE INFO

Article history:
Received 21 June 2021
Received in revised form 18 October 2021
Accepted 26 October 2021
Available online 14 November 2021

Keywords:
Multiple pitching foils
Immersed boundary method
Thrust augmentation
Vortex dynamics
Coherent/branched wake

ABSTRACT

Numerical studies are presented on the propulsive performance and vortex dynamics of multiple hydrofoils pitching in an in-line configuration. The study is motivated by the quest to understand the hydrodynamics of multiple fin-fin interactions in fish swimming. Using the flow conditions (Strouhal and Reynolds numbers) obtained from a solitary pitching foil of zero net thrust, the effect of phase differences between neighboring foils on the hydrodynamic performance is examined both in position-fixed two- and three-foil systems at Reynolds number Re = 500. It is found that the threefoil system achieves a thrust enhancement up to 118% and an efficiency enhancement up to 115% compared to the two-foil system. Correspondingly, the leading-edge vortex (LEV) and the trailing-edge vortex (TEV) of the hindmost foil combine to form a '2P' wake structure behind the three-foil system with the optimal phase differences instead of a '2S' wake, a coherent wake pattern observed behind the optimal two-foil system. The finding suggests that a position-fixed three-foil system can generate a '2P' wake to achieve the maximum thrust production and propulsive efficiency simultaneously by deliberately choosing the undulatory phase for each foil. When increasing Reynolds number to 1000, though the maximum thrust and propulsive efficiency are not achieved simultaneously, the most efficient case still produces more thrust than most of the other cases. Besides, the study on the effects of three-dimensionality shows that when the foils have a larger aspect ratio, the three-foil system has a better hydrodynamic performance, and it follows a similar trend as the two-dimensional (2D) foil system. This work aids in the future design of high-performance underwater vehicles with multiple controlled propulsion elements.

© 2021 Elsevier Ltd. All rights reserved.

1. Introduction

Many fishes swim by oscillating their fins, and complex interactions between multiple fins on a fish have received considerable attention. As a two-foil system, the caudal fin was experimentally observed to interact with the vortices shedding from the upstream dorsal fin of a swimming bluegill sunfish (Drucker and Lauder, 2001; Tytell, 2006), rainbow trout (Drucker and Lauder, 2005) and brook trout (Standen and Lauder, 2007). Using fish-like models and high-fidelity three-dimensional (3D) flow simulations, Liu et al. studied the interactions between the dorsal and caudal fins in jackfish steady swimming, and found that, by interacting with the vortices shed from the upstream fins, the caudal fin achieves a 13.4% increase in thrust production (Liu et al., 2017). Zhong et al. also found that the swimming speed and swimming

E-mail address: hd6q@virginia.edu (H. Dong).

^{*} Corresponding author.

economy increase by up to 15% and 50%, respectively, due to the interactions between the tandem fins in a tuna-like swimming (Zhong et al., 2019). More recently, with a 3D bluegill sunfish model, Han et al. investigated the effects of the dorsal/anal fin flapping phase on the caudal fin hydrodynamic performance and showed that phase-advanced dorsal and anal fins lead to higher propulsive efficiency, while phase-lag dorsal and anal fins result in larger caudal fin thrust production (Han et al., 2020).

Experimental and computational studies on modeled tandem foil system have shown that the system can achieve its optimal propulsive performance by setting the correct phase difference between foils. Akhtar et al. numerically investigated the hydrodynamics of a 2D tandem foil system and examined the effect of the phase difference between the upstream foil and the downstream foil. They reported that, with deliberately tailored phase difference, the upstream foil wake stalls the downstream foil's leading-edge vortex (LEV) and induces a threefold thrust enhancement and a twofold efficiency enhancement on the downstream foil (Akhtar et al., 2007). Using 2D flow simulations, Broering and Lian studied the hydrodynamic performance of a two-foil system, with the phase difference between fore and hind foils changing from 0° to 180°, and found that the thrust and propulsive efficiency of the hind foil were increased by up to 237% and 40%, respectively, as compared to one single foil (Broering and Lian, 2012). They also pointed out that changing the spacing between tandem foils has a similar effect as that of changing the phase difference between those foils. Later, detailed research has been done on investigating the wake structures behind tandem foils. Using two hydrofoils pitching in-line. Boschitsch et al. experimentally investigated the effect of phase difference over a broader range, from 0° to 360°, and found up to 160% enhancement in thrust and 150% increase in propulsive efficiency (Boschitsch et al., 2014). They suggested that the enhanced and diminished performances were attributed to coherent and branched interaction modes, respectively. In addition, the effects of three-dimensionality in the two tandem foils were experimentally studied by Kurt and Moored, and it was found that, instead of correlating with the maximum and minimum propulsive efficiency, in 3D cases, the coherent and branched wake modes are only related to the peak thrust and minimum power, respectively (Kurt and Moored, 2018).

Nevertheless, the hydrodynamics of multiple-fin tandem systems have yet received enough attention. Kinematics analysis and flow visualization showed that rainbow trout can actively oscillate pelvic fins at slow swimming speed, and the pelvic fin wake alters the anal fin angle of attack and influences the upstream flow of the caudal fin (Standen, 2010), which can be modeled as a three-fin system, where all fins oscillate in-line. Besides, Maia et al. examined the hydrodynamics of two dorsal fins in bamboo shark and proposed that both dorsal fins actively contribute thrust production during steady swimming and can be considered as propulsive appendages in a tandem configuration with caudal fin (Maia et al., 2017). Recently, Wang et al., using a combined experimental and computational method, investigated the hydrodynamics of five oscillating finlets in yellowfin tuna swimming and found that the total drag of the five assembly was reduced by 21.5% due to the interactions among these finlets, which indicated the important role of interactions between multiple fins in underwater propulsion (Wang et al., 2020). Our previous research on the propulsive performance of multiple tandem hydrofoils suggested that, by choosing appropriate phase difference, the propulsive performance of the three-foil pitching in-line system has been enhanced significantly compared to a similar two-foil system (Yuan et al., 2015). If the number of foils increases, the maximum collective thrust and efficiency of the systems gradually reaches a plateau.

In this work, we perform a comprehensive analysis on the wake structures, force production and hydrodynamic efficiency of three tandem foils pitching in-line over a range of phase difference from 0° to 360°. The effects of Reynolds number (*Re*) and three-dimensionality on the propulsive performance and wake structures are also studied. The primary motivation is to provide fundamental insights into the fluid dynamics of interactions between multiple pitching foils and supplement the extensive works that have been done in the past on two-dimensional tandem foils, which will not only help to design isolated underwater vehicles but also guide the arrangement of underwater robot swarms (Pan and Dong, 2020; Peng et al., 2018; Xu et al., 2017). We begin by discussing the hydrodynamics of a solitary foil in zero-net-thrust pitching. This is followed by presenting results on hydrodynamic performance of multiple foils and a detailed discussion of the wake structures as well as mean wake features observed over the range of the parameters varied in the current study. Finally, the effects of Reynolds number and three-dimensionality on the performance and wake structures are presented.

2. Problem definition and numerical approach

2.1. Problem definition

In the present research, all hydrofoils share the same shape, with a round leading edge and a tapered trailing edge (see Fig. 1). The diameter of the round leading edge D is set to be D/C = 0.1, where C is the chord length. The foils are placed in an in-line configuration undergoing a prescribed periodic pitching motion and the pitching angle θ_i of the ith foil is defined in Eq. (1),

$$\theta_i(t) = \theta_0 \cos(2\pi f t + \varphi_i) \tag{1}$$

where θ_0 is the pitching amplitude, f is the flapping frequency, t is time, and φ_i is the initial phase of the ith foil. In Eq. (1), the pitching amplitude θ_0 is set to be 7.56°, which results in a foil tip peak-to-peak amplitude $A = 2(C - D/2)\sin\theta_0 \approx$

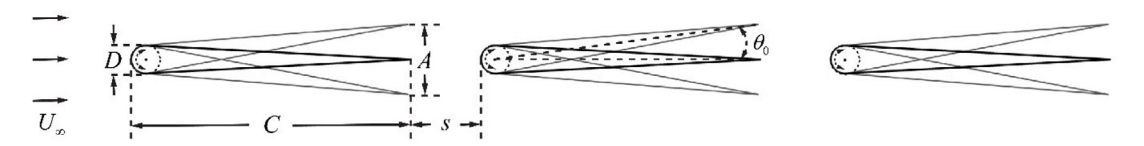


Fig. 1. Schematic of the three tandem foil system. The relevant parameters are the chord length C, the round leading edge diameter D, the streamwise spacing s, foil tip peak-to-peak amplitude A and the pitching amplitude θ_0 .

0.25C and φ_1 is always set as 0°. Based on the definition of φ_i , the phase difference between the *i*th and *j*th foil is defined as φ_{i-j} , where

$$\varphi_{i-i} = \varphi_i - \varphi_i. \tag{2}$$

The dimensionless spacing s between adjacent foils is set to be s/C = 0.25, and Boschitsch et al. suggested that the downstream foil has the strongest influence on the propulsive performance of the upstream foil in an in-line configuration at this distance (Boschitsch et al., 2014). Since previous work has made the conclusion that changing the phase difference has a similar effect as changing the spacing (Broering and Lian, 2012; Kurt and Moored, 2018), in current study, to focus on the wake structure interactions, all the simulations are conducted with s fixed and φ_{i-j} ranging from 0° to 360°.

The tandem foil system is placed in an incompressible viscous flow with a constant incoming velocity U_{∞} . Two dimensionless parameters, the foil tip peak-to-peak amplitude based Strouhal number St and chord length based Reynolds number Re, are used to characterize the flow conditions:

$$St = \frac{fA}{U_{\infty}}, Re = \frac{CU_{\infty}}{v}, \tag{3}$$

where ν is the kinematic viscosity.

In the current study, to limit the grid requirement, two Re numbers, 500 and 1000 are used, which are comparable to that adopted by previous works (Lewin and Haj-Hariri, 2003; Akhtar et al., 2007). And later, in Section 3.1, based on the simulation results of solitary foil, St = 0.25 is chosen for the subsequent multiple-foil system simulations, which is in the range where swimming fish achieves optimal propulsion performance (Triantafyllou et al., 1993).

To evaluate the performance of the individual foils, cycle-averaged thrust coefficient $\overline{C}_{T,i}$, power coefficient $\overline{C}_{P,i}$ and propulsive efficiency n_i are defined for the ith foil,

$$\overline{C}_{T,i} = \frac{\overline{T}_i}{0.5\rho U_{\infty}^2 C^2}, \overline{C}_{P,i} = \frac{\overline{P}_i}{0.5\rho U_{\infty}^3 C^2}, \eta_i = \frac{\overline{C}_{T,i}}{\overline{C}_{P,i}}, \tag{4}$$

with the fluid density denoted by ρ and cycle-averaged thrust and hydrodynamic power of the *i*th foil denoted by \overline{P}_i , respectively. When \overline{T}_i value is negative, it corresponds to drag production. Here, the force T_i is calculated by direct integrations of the surface pressure and shear, which are projected from the flow variables around the foil, over the foil surface. The power P_i is calculated as:

$$P_i = \oint -(\overline{\sigma} \cdot \mathbf{n}) \cdot V ds, \tag{5}$$

where \oint represents the integration along the foil surface, $\overline{\sigma}$ and V denote the stress tensor and the velocity vector of the fluid adjacent to the foil surface, respectively. V is the local velocity on the foil surface. And n is the normal vector of each point on the foil surface.

To evaluate the performance of the propulsion system, the collective thrust coefficient \overline{C}_T , power coefficient \overline{C}_P and propulsive efficiency $\overline{\eta}$ are defined for the system as:

$$\overline{C}_T = \frac{\sum_{i=1}^N \overline{T}_i}{0.5N\rho U_\infty^2 C^2}, \overline{C}_P = \frac{\sum_{i=1}^N \overline{P}_i}{0.5N\rho U_\infty^3 C^2}, \overline{\eta} = \frac{\overline{C}_T}{\overline{C}_P}$$

$$(6)$$

where N is the total number of hydrofoils.

To investigate the wake structure interactions, the instantaneous vorticity (ω) and time-averaged streamwise velocity (\overline{U}) are plotted in the flow field. Please be noted that, they both are dimensionless variables, and are normalized by (U_{∞}/C) and U_{∞} respectively.

2.2. Numerical method and grid independent study

The 2D incompressible Navier-Stokes equations are used as the governing equations, written in the form as:

$$\frac{\partial u_i}{\partial x_i} = 0; \frac{\partial u_i}{\partial t} + \frac{\partial u_i u_j}{\partial x_j} = -\frac{\partial p}{\partial x_i} + \frac{1}{Re} \frac{\partial^2 u_i}{\partial x_j \partial x_j}$$
 (7)

where u_i is the velocity component and p is the pressure.

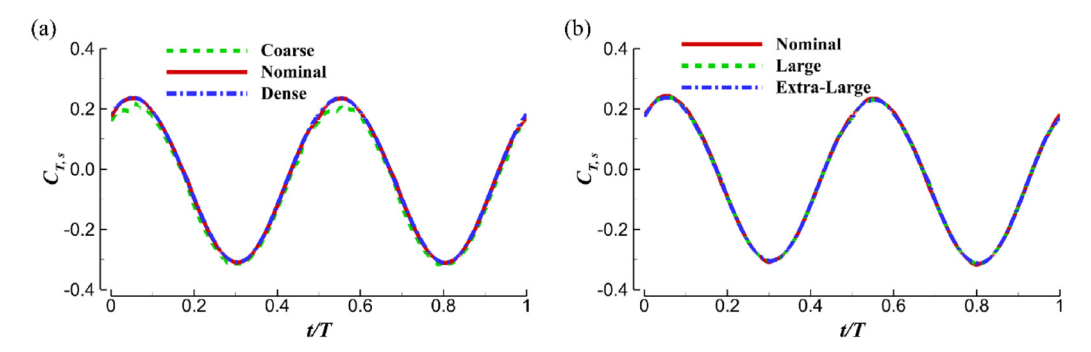


Fig. 2. Grid and domain independence study. (a) Comparison of the thrust coefficient of a solitary foil pitching at St=0.25 and Re=500 using coarse, nominal and dense grids. The grids employed in the simulations are coarse grid (565×129) with the highest grid resolution $(\Delta x=0.0125C, \Delta y=0.0038C)$, nominal grid (1025×225) with the highest grid resolution $(\Delta x=0.0063C, \Delta y=0.0039C)$, and dense grid (2025×417) with the highest grid resolution $(\Delta x=0.0031C, \Delta y=0.0020C)$. (b) Thrust coefficient histories calculated from three different domain sizes with the same grid resolution. The nominal domain is $15C \times 6C$. The large domain is $15C \times 12C$. The extra-large domain is $30C \times 12C$.

The governing equations are discretized in space using a cell-centered, collocated (non-staggered) arrangement of the primitive variables (u_i and p), and solved using a finite-difference-based Cartesian grid immersed boundary method (Mittal et al., 2008). These equations are integrated in time using the fractional step method (Van Kan, 1986). This method has been successfully applied to simulate many biological flapping propulsions (Han et al., 2020; Khalid et al., 2021; Li and Dong, 2016; Liu et al., 2017; Pan and Dong, 2020).

For all the 2D flow simulations, similar to the setup used in work (Van Buren et al., 2019), at the inflow boundary, a constant velocity incoming flow boundary condition is given, and at the outflow boundary, a zero gradient boundary condition is employed on the streamwise velocity to let the vortices to convect out of the boundary. And for the two lateral boundaries, zero gradient boundary condition is used for the velocity. For the pressure at all the boundaries here, homogeneous Neumann boundary conditions are used. Based on our previous experience on similar simulations (Yuan et al., 2015), a $15C \times 6C$ non-uniform Cartesian grid is employed for the whole flow domain. A refined zone with size $7.20C \times 1.46C$ is used to capture detailed wake structures, and around the pitching foil, an extremely dense region with size $4.00C \times 0.26C$ is deployed to resolve the boundaries of the foil accurately. Simulations on a solitary foil pitching at St = 0.25, Re = 500 are conducted to test the grid and domain independence. Fig. 2(a) compares the instantaneous thrust coefficients of the pitching foil calculated from three different grids (coarse, nominal and fine grids), and the result shows that the difference of the thrust coefficient peak values between the nominal grid and the dense grid is less than 1%. And with the same flow condition and same mesh resolution around the pitching foil, simulations are run with three different domain sizes. As can be seen in Fig. 2(b), compared to the nominal domain size used here $(15C \times 6C)$, the large $(15C \times 12C)$ and extra-large $(30C \times 12C)$ domains lead to a less than 2.1% difference in thrust coefficient peak value. Thus, the grid dependence and domain dependence are precluded, and the nominal grid and domain here are chosen for all the 2D simulations.

To validate the flow solver and simulation set-up, simulations are conducted on solitary and two tandem foils in pitching at Re = 4700 to compare the results with previously reported experimental data (Boschitsch et al., 2014). Fig. 3(a) compares the thrust coefficients of the solitary pitching foil between the experiments and simulations at different St when Re = 4700. For solitary foil, the variation trend and magnitude of the thrust production calculated by the current solver were in reasonably good agreement with the experiments. And further, in Fig. 3(b), at St = 0.25, with streamwise foil distance s/C = 0.25, the normalized cycle-averaged thrust of the downstream foil in the two tandem foil configuration was shown. With phase difference φ ranging from 0° to 360°, the comparison between the simulations and experimental data confirms the validity of current CFD solver in calculating the hydrodynamic performance of tandem foil systems. Fig. 3(c) shows the wake structure obtained from the simulations with St = 0.25, s/C = 0.25 and $\varphi = 180^{\circ}$. A vortex pair (vortices 1 and A_L) is generated between the two foils and travels transversely away from the foils when it moves downstream. Vortices 2 and B_I denote the vortex pair from the last stroke and show a lateral distance about 0.5C from the centerline of the downstream foil. Meanwhile, a negative vortex, which is denoted as 'A', is shedding from the trailing edge of the downstream foil. 'B' is the positive trailing edge vortex from the last half stroke. Between vortex A and B, a 0.5C streamwise distance is observed, which is corresponding to the reduced frequency $f^* = 1.0$ in the simulation. Referring to Fig. 15 in Ref. Boschitsch et al. (2014), our simulation results have captured identical vortex wakes as recorded in the experiments, which indicates that the current CFD solver performed well in computing both near wake and far wake structures. In addition, Fig. 3(d) presents the wake structures at St = 0.25, s/C = 0.25 and $\varphi = 0^{\circ}$, which also shows good agreement with the experimental results (Boschitsch et al., 2014).

3. Results and discussion

In Section 3.1, the propulsive performance of a solitary pitching foil is shown first. Based on the results, St = 0.25 is chosen for the baseline case, which corresponds to the net-zero thrust generation. And then, in Section 3.2, the propulsive

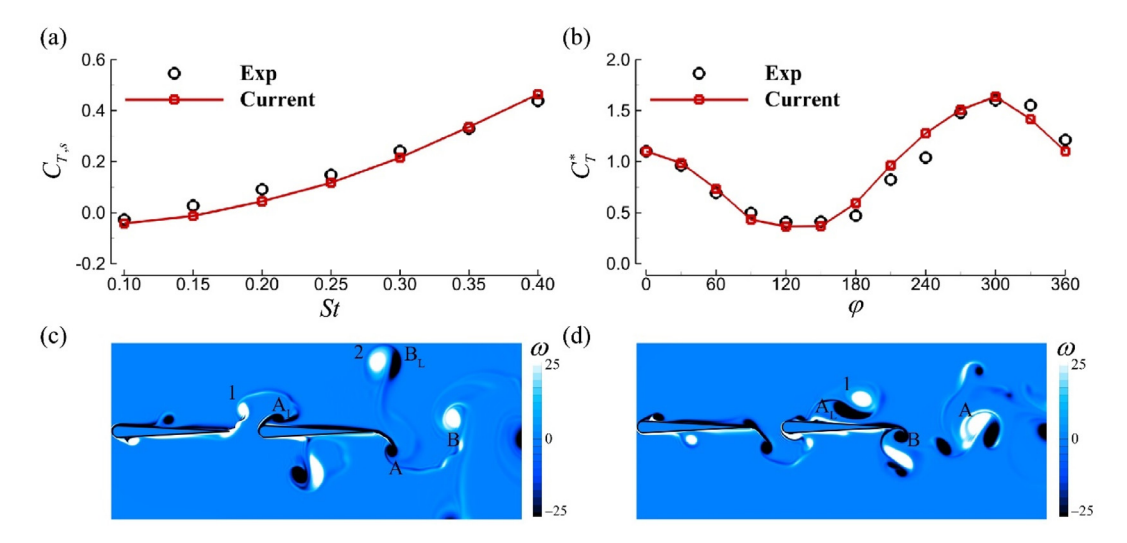


Fig. 3. (a) Thrust coefficient $(C_{T,s})$ of solitary foil pitching at different St and (b) normalized cycle-averaged thrust coefficient (C_T^*) of downstream foil in a two tandem foil configuration pitching at St = 0.25, Re = 4700 from current simulations and experimental (Exp) measurements (Boschitsch et al., 2014). Vorticity contours of two tandem foils pitching at St = 0.25, Re = 4700 with streamwise distance s/C = 0.25 and phase difference (c) $\varphi = 180^\circ$ and (d) $\varphi = 0^\circ$.

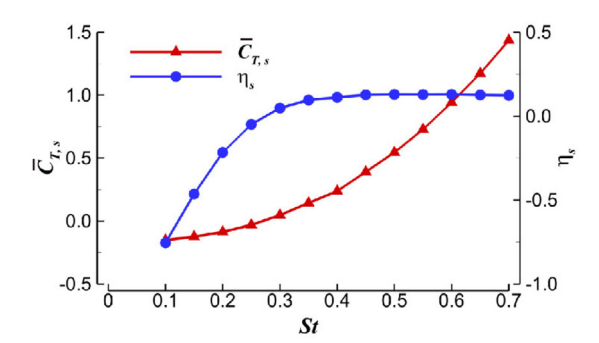


Fig. 4. Cycle-averaged thrust coefficient $\overline{C}_{T,s}$ and propulsive efficiency η_s of a solitary pitching foil at different Strouhal numbers, with Re=500.

performance and wake structures of a two-foil system are studied with the phase differential φ_{2-1} ranging from 0° to 360°. In Section 3.3, a three-foil system is investigated. The hydrodynamic performance and vortex wake are mapped out in a phase diagram. And the formations of different vortex wakes are discussed in detail. The effects of Reynolds number and three-dimensionality are discussed in Sections 3.4 and 3.5, respectively.

3.1. Solitary foil: propulsive performance and wake dynamics

The propulsive performance of a solitary pitching foil is considered first, which is denoted by the subscript 's'. The cycle-averaged thrust coefficient $\overline{C}_{T,S}$ and propulsive efficiency η_S of this solitary foil at different St are plotted in Fig. 4. From Fig. 4, it is observed that, with the increase of St, the thrust coefficient of this pitching foil increases monotonically, which is similar to the previous work (Boschitsch et al., 2014). When $St \leq 0.25$, the thrust coefficient of the pitching foil is negative, which implies drag force generation. And when St > 0.25, the pitching foil starts to generate thrust. From St = 0.10 to 0.45, the propulsive efficiency of the pitching foil rises from -75.5% to 12.7%. And then, it reaches a plateau and remains at around 12.7%.

As shown in Fig. 4, at St = 0.25, the cycle-averaged thrust coefficient, \overline{C}_T , is -0.031 and the cycle-averaged power coefficient, \overline{C}_P , is 0.631. It is worth to note that the magnitude of \overline{C}_T is about 6% of its instantaneous thrust force peak-to-peak amplitude (Fig. 2). This case is chosen as our baseline setup for studying two foils and three foils in the following sections. During each oscillation period, the thrust coefficient exhibits half-cycle periodicity due to the symmetric pitching motion, as shown in Fig. 2. The peaks of thrust happen at t = 0.05T, 0.55T, when the tip of the pitching foil just reaches its lateralmost position and starts to pitch back. Fig. 5 shows the corresponding instantaneous vorticity contour and time-averaged streamwise velocity field of the baseline case. A classic reverse von Kármán vortex street, which is characterized by an array of opposite signed vortices, is formed behind the oscillating foil, in Fig. 5(a). Based on the work (Williamson and

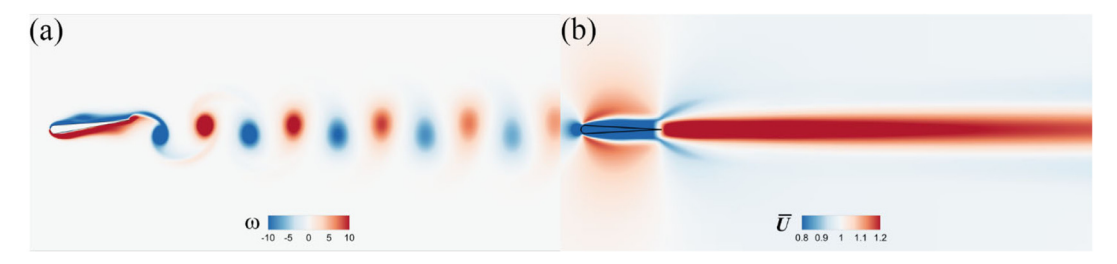


Fig. 5. (a) Instantaneous vorticity contour and (b) time-averaged streamwise velocity field of a solitary foil pitching at St = 0.25, Re = 500.

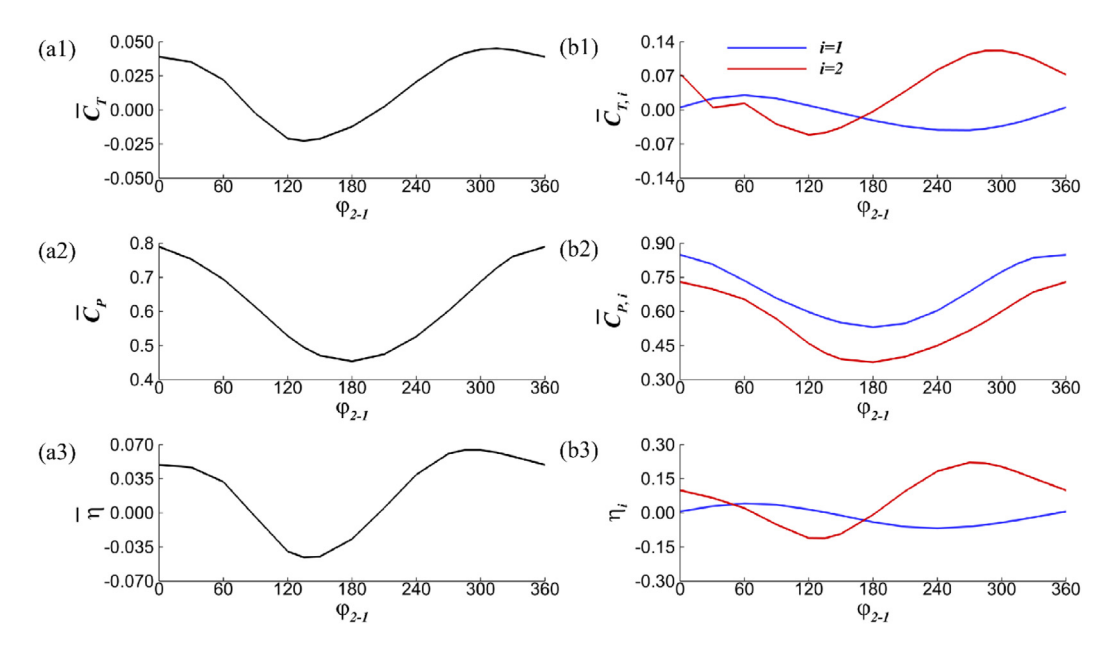


Fig. 6. Propulsive performance of the two tandem foil system with respect to φ_{2-1} is shown in (a1-a3): (a1) collective cycle-averaged thrust coefficient, (a2) collective cycle-averaged power coefficient and (a3) collective propulsive efficiency. The propulsive performance of each individual foil is shown in (b1-b3): (b1) cycle-averaged thrust coefficient, (b2) cycle-averaged power coefficient and (b3) propulsive efficiency. The blue lines denote the upstream foil and the red lines denote the downstream foil. (For interpretation of the references to color in this figure legend, the reader is referred to the web version of this article.)

Roshko, 1988), this reverse von Kármán vortex street is described as a '2S' structure. And attributed to this '2S' structure, a concentrated high momentum downstream jet is formed at the centerline of the wake.

3.2. Two tandem foil system: propulsive performance and wake dynamics

In this section, two pitching foils are arranged in line with the streamwise distance *s* fixed to be 0.25*C*. By changing the phase difference, the related propulsive performance and vortex wakes are studied.

3.2.1. Propulsive performance

The propulsive performance of the two tandem foil system is shown in Fig. 6. From Fig. 6(a1-a3), where the collective performance is shown, it is observed that when the second foil is involved, the system starts to generate thrust at certain phase differences. Among all these cases, the largest propulsive efficiency ($\bar{\eta}=6.5\%$) happens when $\varphi_{2-1}=300^\circ$, with $\bar{C}_T=0.044$, $\bar{C}_P=0.687$, and this case is defined as the optimal case of the two-foil system. The magnitude of \bar{C}_T of this case ($\varphi_{2-1}=300^\circ$) is about 8.6% of the peak-to-peak amplitude of the instantaneous thrust force of a solitary pitching foil. Correspondingly, the smallest efficiency ($\bar{\eta}=-4.6\%$) happens when $\varphi_{2-1}=135^\circ$, with $\bar{C}_T=-0.023$, $\bar{C}_P=0.495$, and this case is defined as the worst case. The performance of each individual foil is shown in Fig. 6(b1-b3). In Fig. 6(b1), compared to the upstream foil, a much larger peak thrust is observed on the downstream foil. The peak thrust coefficient of the downstream foil is 0.122 while that of the upstream foil is 0.030. Furthermore, the changing tendencies of these two foils are opposite. When the thrust of the downstream foil reaches its maximal value, the thrust of the upstream foil is almost at its trough value. This is because, in the near-wake configuration, a detrimental effect is induced for the upstream foil thrust generation due to the presence of the low-pressure suction zone at the leading edge of the downstream foil

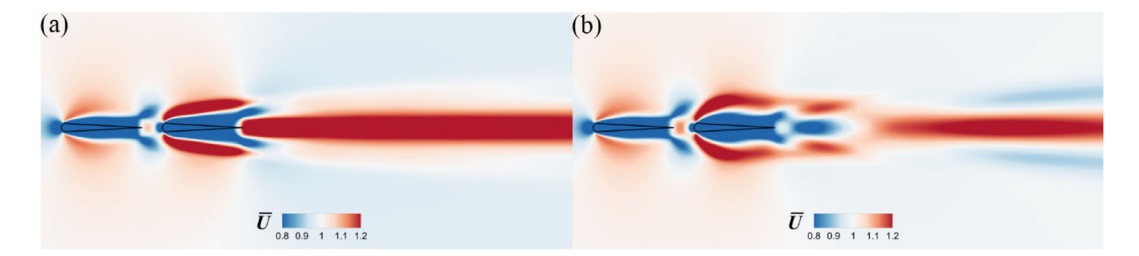


Fig. 7. Time-averaged streamwise velocity fields of two tandem foil system with phase differences: (a) $\varphi_{2-1} = 300^\circ$ (best performance), (b) $\varphi_{2-1} = 135^\circ$ (worst performance).

(Boschitsch et al., 2014). To the contrary of the thrust generation, in Fig. 6(b2), similar changing tendencies are observed on the power coefficients of these two tandem foils, and the power consumption of the downstream foil is always lower than that of the upstream foil. For both foils, the lowest power consumption happens when $\varphi_{2-1} = 180^{\circ}$ while the largest power consumption happens when $\varphi_{2-1} = 0^{\circ}$. Considering the larger thrust generation and lower power consumption of the downstream foil, we can draw the conclusion that, the collective efficiency of the two tandem foil system is mainly determined by the downstream foil, as shown in Fig. 6(b3).

3.2.2. Wake dynamics

In this section, comparisons are made between the best and worst cases on the wake dynamics to give us a better understanding of the performance difference.

In Fig. 7, the time-averaged streamwise velocity fields of these two cases are plotted. Two angled jets can be found for both cases at the anterior part of the downstream foil. However, case $\varphi_{2-1} = 135^{\circ}$ (Fig. 7(b)) shows a larger transverse distance between the angled jet and the edge of the downstream foil than the case $\varphi_{2-1} = 300^{\circ}$ (Fig. 7(a)). Fig. 7 also shows that, compared to the strong coherent downstream jet generated in the case $\varphi_{2-1}=300^\circ$, a branched jet is characterized in case $\varphi_{2-1} = 135^{\circ}$ at the near wake field, where a lower mean velocity region can be found right behind the downstream foil. At the far-field, both cases show a coherent momentum jet. To explore the formation of these two specific downstream jets, the evolution of the vorticity field is shown in Fig. 8. In Fig. 8(a1, b1), for both cases, when the upstream foil is pitching down from its mid-position, a strong counter-clockwise vortex is formed at its trailing edge, which is denoted as A_2 . In Fig. 8(a2, b2), the shedding vortex A_2 moves downstream and arrives at the leading edge of the downstream foil. Meanwhile, a noticeable clockwise leading-edge vortex, which is denoted as B_1 in Fig. 8(a2, b2), is generating at the downstream foil leading edge. Then, A_2 and B_1 , they two form a vortex pair and move downstream together. In Fig. 8(a3, a4), when $\varphi_{2-1} = 300^{\circ}$, due to the motion of the pitching foil, the formed vortex pair rolls along the side of the foil, while at the same time, in Fig. 8(b3, b4), when $\varphi_{2-1} = 135^{\circ}$, the vortex pair starts to travel transversely away from the pitching foil. Compared to the case $\varphi_{2-1}=300^\circ$, the lateral distance between the vortex pair and the downstream foil edge is much larger when $\varphi_{2-1}=135^\circ$. Because of this, the vortex pairs of these two cases interact with the downstream foil trailing-edge vortex in two different ways. In Fig. 8(a1), when the vortex pair A'_2 and B'_1 , where the superscript '' denotes the vortex generated during the last oscillation period, arrives at the trailing edge of the downstream foil, a large vortex B_2 just sheds off from the downstream foil trailing edge. B'_1 follows B_2 and forms a stretched trail after B_2 . During this time, vortex A'_2 attenuates quickly and only a reverse von Kármán vortex street is left behind the downstream foil. Meanwhile, in Fig. 8(b2), because of the pitching phase of the downstream foil, A'_2 and B'_1 pass the trailing edge of the downstream foil already when the vortex B_2 comes into being. From Fig. 8(b2, b3), it is observed that, B'_1 and B_2 merge into each other at a position which is about 0.36C away from the trailing edge of the downstream foil. And the formed vortex generates a flow jet pointing upstream with the vortex structures at the trailing edge of the downstream foil, as the arrow in Fig. 8(b4) shows. Finally, a '2S' wake pattern is formed, and its strength is much weaker than that of the case $\varphi_{2-1} = 300^{\circ}$.

The above comparisons show that, when $\varphi_{2-1}=135^\circ$, the vortex pair advects away from the centerline of the pitching foil, and this explains why in Fig. 7(b), the lateral distance between the angled jet and the downstream foil edge is larger than that in Fig. 7(a). Furthermore, when $\varphi_{2-1}=135^\circ$, the lower mean velocity region right after the downstream foil is attributed to the interactions between the vortex pair and the trailing-edge vortex. In the far-field, both cases exhibit a '2S' wake structure and this corresponds with the coherent high momentum jet.

3.3. Three tandem foil system: propulsive performance and wake dynamics

In this section, the performance of three tandem foil system is explored first. The neighboring foil phase differences φ_{2-1} and φ_{3-2} are varied between 0° and 360° with a spacing of every 10° generating a total of 1296 cases. It is found that, a net increase in the collective propulsive performance can be achieved by introducing one more foil to the aforementioned two tandem foil system. The evolution of the vortex wakes is studied to understand the underlying mechanisms and the related wake structures are mapped out in a phase diagram.

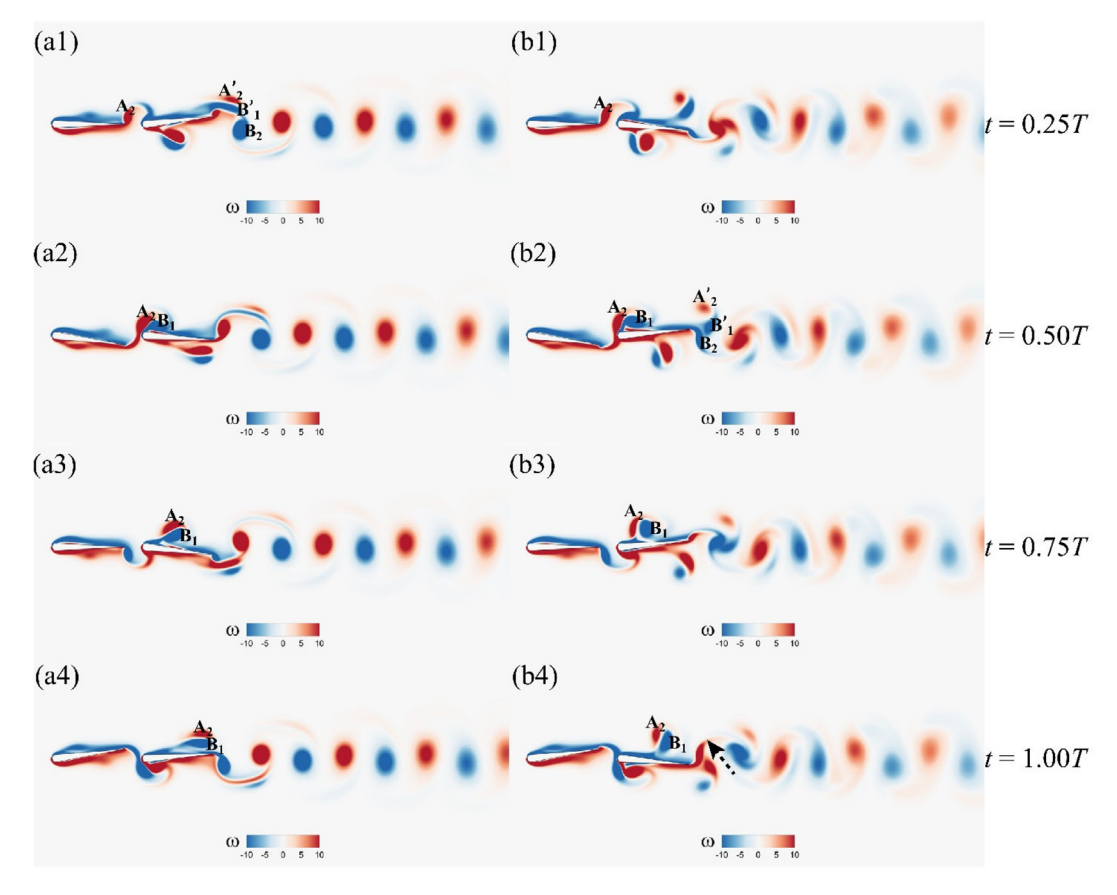


Fig. 8. Evolutions of the vortex structures in one oscillation period for the optimal case $\varphi_{2-1}=300^\circ$ (a1-a4) and the worst case $\varphi_{2-1}=135^\circ$ (b1-b4).

3.3.1. Propulsive performance overview of the three tandem foil system

Fig. 9 presents the collective thrust coefficient and propulsive efficiency of the three tandem foil system. In Fig. 9(b), the peak value of the efficiency happens at $(\varphi_{2-1}=300^\circ,\varphi_{3-2}=320^\circ)$, which is defined as the optimal case, and the trough value happens at $(\varphi_{2-1}=180^\circ,\varphi_{3-2}=150^\circ)$, which is defined as the worst case. The collective thrust coefficient shares a similar trend with the collective efficiency, with its maximum value happens at $(\varphi_{2-1}=310^\circ,\varphi_{3-2}=320^\circ)$ and minimum value happens at $(\varphi_{2-1}=170^\circ,\varphi_{3-2}=150^\circ)$. This kind of similar distributions between \overline{C}_T and $\overline{\eta}$ are due to that, with the change of the phase difference, the relative change of the power consumption is smaller than that of the thrust production. The collective thrust coefficient and propulsive efficiency of the optimal and the worst cases are $\overline{C}_{T,optimal}=0.096$, $\overline{\eta}_{optimal}=14.0\%$ and $\overline{C}_{T,worst}=-0.003$, $\overline{\eta}_{worst}=-0.6\%$, respectively. Compared to the optimal case of the two tandem foils $(\varphi_{2-1}=300^\circ,\overline{C}_T=0.044,\overline{\eta}=6.5\%)$, the three-foil system achieves a thrust enhancement up to 118% and an efficiency enhancement up to 115% with the optimal phase difference. The magnitude of \overline{C}_T of this case is about 18.4% of the peak-to-peak amplitude of the instantaneous thrust force of a solitary pitching foil. Here, the worst case is still drag producing, but the collective drag force is very small, which is about one-eighth of the worst case in the two-foil system $(\varphi_{2-1}=135^\circ, \overline{C}_T=0-0.023, \overline{\eta}=-4.6\%)$.

3.3.2. Wake dynamics of the three tandem foil system

Four different wake types, including '2S' von Kármán vortex, '2S' reverse von Kármán vortex, '2P' and '2P + 2S' vortex structures, are observed and mapped out in Fig. 10. The '2S' wake structure dominates a large region in the parameter domain and the inferior performance region in Fig. 9 is mainly related to the '2S' von Kármán vortex street. Most of the thrust generation cases express a '2S' reverse von Kármán vortex street or a '2P' vortex and the high-performance region in Fig. 9 is mainly featured by the '2P' vortex structure. '2P + 2S' wake structures are also observed in the simulations, which corresponds to a moderate performance region in Fig. 9.

To look into the formation of different wake patterns, in Fig. 11, φ_{2-1} is fixed to be 300° and the instantaneous vorticity fields as well as the time-averaged streamwise velocity fields of cases with different φ_{3-2} are shown. With φ_{3-2} ranging from 0° to 360°, the streamwise mean velocity distribution changes a lot in Fig. 11(b1-b6). In Fig. 11(b1), when

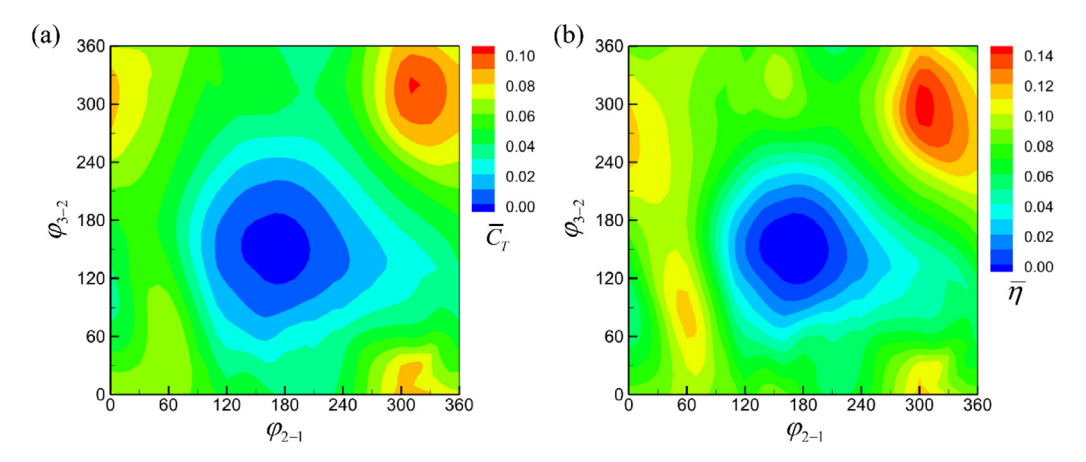


Fig. 9. Propulsive performance of the three tandem foil system at Re = 500: (a) the collective thrust coefficient and (b) the collective propulsive efficiency.

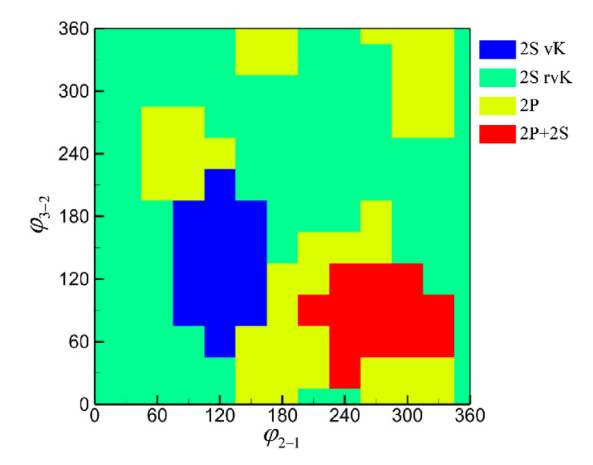


Fig. 10. Phase diagram of vortex wakes with respect to the phase differentials φ_{2-1} and φ_{3-2} . 'vK' is for von Kármán vortex street and 'rvK' is for reverse von Kármán vortex street.

 $\varphi_{3-2}=60^\circ$, two branches of high momentum jets are observed to start from the leading edge of the hindmost foil and then converge into each other at a downstream point, which is about 2.0C away from the trailing edge of the hindmost foil, and form a coherent jet. In this case, the hindmost foil is surrounded by a lower velocity region and the coherent high momentum jet can only be found in the far-wake field. In Fig. 11(b2), when phase difference φ_{3-2} is increased to 120°, instead of the coherent far-field high momentum jet observed in Fig. 11(b1), in the studied flow domain, the time-averaged streamwise velocity field is characterized by a pair of oblique high momentum jets, which start at the leading edge of the hindmost foil. If the phase difference keeps increasing, the far-field high momentum jet reappears and at the same time, two branches of high momentum jets show up right after the trailing edge of the hindmost foil, as shown in Fig. 11(b3). And then, when $\varphi_{3-2}=240^\circ$, all these high momentum jets will merge together and form one concentrated downstream jet, which corresponds to the thrust improvement in Fig. 9(a). However, it is noticed from Fig. 9 that further increase in φ_{3-2} brings a further enhancement in propulsive performance. When $\varphi_{3-2}=300^\circ$, larger thrust and efficiency are achieved and the branched high momentum jets are observed in Fig. 11(b5). However, if we compare this to the branched high momentum jets in Fig. 11(b2), which start from the leading edge of the hindmost foil, in Fig. 11(b5), the branched wake starts right behind the trailing edge of the hindmost foil. Though the time-averaged streamwise velocity field of the optimal case ($\varphi_{2-1}=300^\circ$, $\varphi_{3-2}=320^\circ$) is not plotted here, it shares a similar structure with Fig. 11(b5). Further increase in φ_{3-2} causes the two high-momentum branches to move away from the centerline and separate from each other. Finally, the two branches connect with the high-velocity regions beside the hindmost foil and form a feeble branched wake mode, as shown in Fig. 11(b6).

Corresponding to those different streamwise velocity fields, the instantaneous vorticity fields are shown in Fig. 11(a1–a6). Similar to the two-foil system with $\varphi_{2-1}=300^\circ$ (Fig. 8(a1–a4)), a vortex pair is observed moving along the second foil and dissipates immediately after it leaves this foil. To focus on the wake structure behind the third foil, this vortex pair in not further looked into, while the vortex structures around the hindmost foil are investigated in detail. When

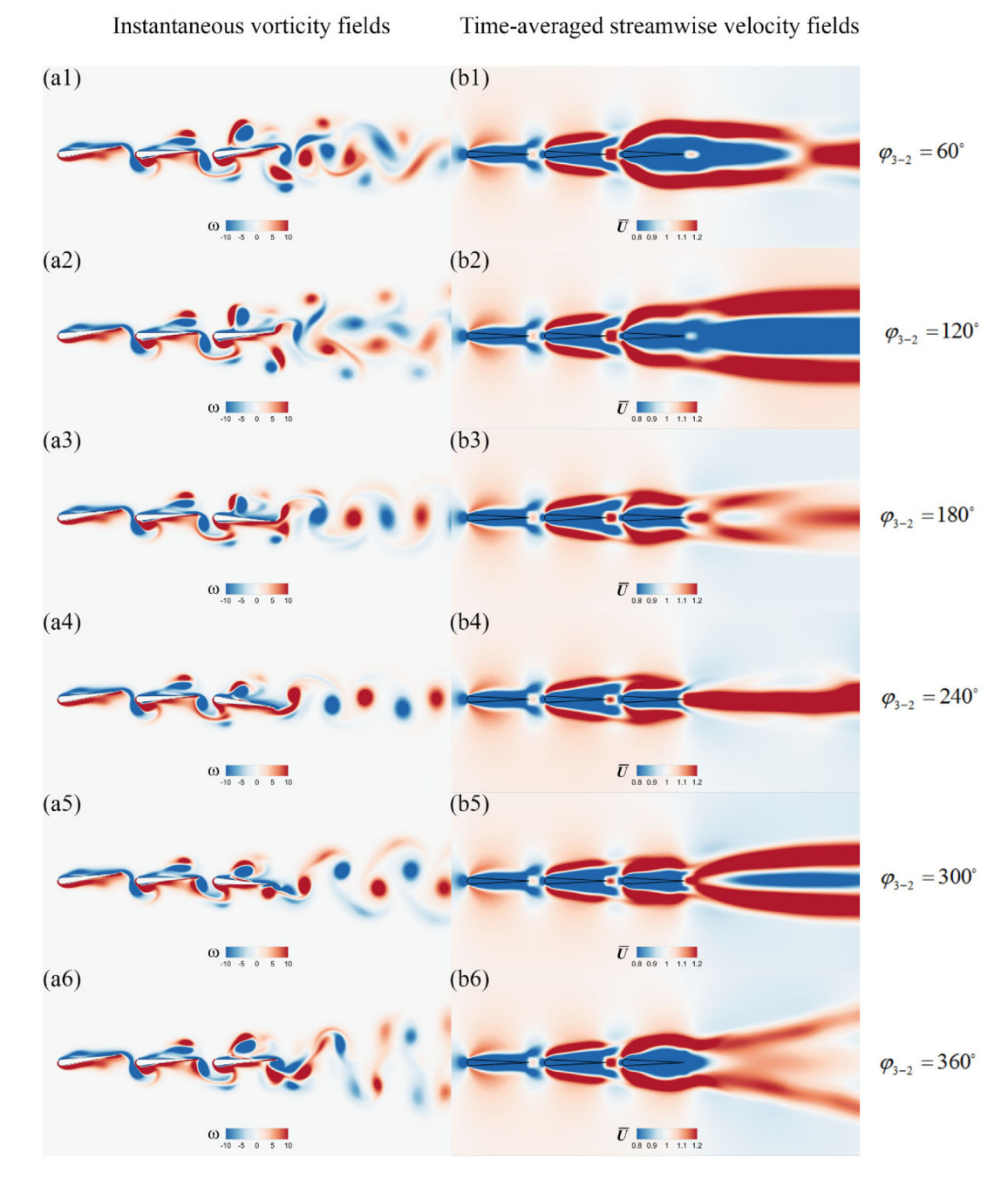


Fig. 11. (a1–a6) Instantaneous vorticity fields and (b1–b6) time-averaged streamwise velocity fields of three tandem foil system with phase differential φ_{3-2} ranging from 0° to 360° and $\varphi_{2-1} = 300^\circ$.

 $\varphi_{3-2} = 60^{\circ}$, 120°, a '2P + 2S' structure shows up in the downstream, where the '2P' part forms at the leading edge of the hindmost foil and moves away from the centerline, and the '2S' part forms at the trailing edge of the same foil and generates a similar layout with the von Kármán vortex street. When $\varphi_{3-2} = 180^{\circ}$, 240°, the vortex pair generated at the hindmost foil leading edge rolls along the edge of the foil and when it arrives at the trailing edge of the foil, the trailing-edge vortex absorbs the like-signed part from the vortex pair and the left opposite-signed part dies down immediately in the wake. Thus, in Fig. 11(a3, a4), only a '2S' wake structure is observed in the downstream.

With further increase in the phase differential, in Fig. 11(a5, a6), when $\varphi_{3-2} = 300^{\circ}$, 360°, a '2P' wake structure is found, which indicates two pairs of vortices from each oscillation stroke. Each vortex pair consists of one vortex from the leading edge of the hindmost foil and the other one from the hindmost foil trailing edge. The formations of '2P + 2S' and

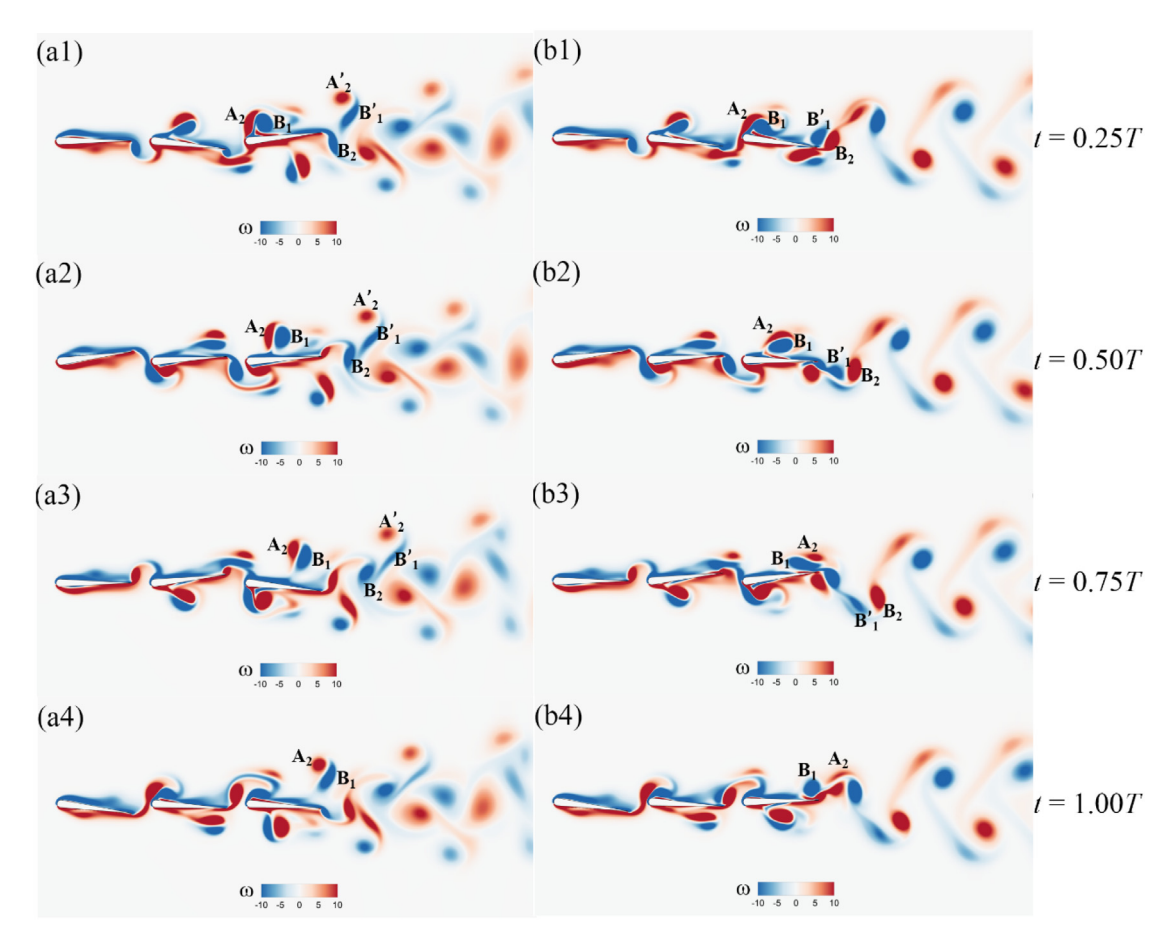


Fig. 12. Evolutions of the vortex structures in one oscillation period for the '2P + 2S' wake (a1-a4), which is formed when $\varphi_{2-1} = 300^{\circ}$, $\varphi_{3-2} = 120^{\circ}$, and the '2P' wake (b1-b4), which is formed when $\varphi_{2-1} = 300^{\circ}$, $\varphi_{3-2} = 320^{\circ}$.

'2P' wake structures are discussed in the following part in detail, while the formation of the '2S' wake structure follows a similar procedure with what happens in the two-foil system and is not discussed here.

3.3.3. Formation of '2P + 2S' and '2P' wakes

Fig. 12 shows the typical vortex formation of the '2P + 2S' wake when $\varphi_{2-1} = 300^{\circ}$, $\varphi_{3-2} = 120^{\circ}$ and the '2P' wake when $\varphi_{2-1}=300^\circ$, $\varphi_{3-2}=320^\circ$. In both cases, the vortex A_2 shedding from the second foil moves downstream and interacts with the hindmost foil leading-edge vortex B_1 (Fig. 12(a1, b1)). They two then form a vortex pair and move downstream together. In Fig. 12(a2-a4), due to the motion of the pitching foil, the formed vortex pair travels transversely away from the foil. When the hindmost foil pitches back from its bottommost position and starts to generate a vortex at its trailing edge in Fig. 12(a4), B_1 has passed the hindmost foil tail tip. And referring back to Fig. 12(a1-a2), when the hindmost foil trailing edge vortex B_2 sheds into the wake, the vortex pair (labeled as A'_2 and B'_1) formed in the last oscillation stroke has moved into the downstream and merely interacts with the formed trailing edge vortex. The trailing edge vortex then forms a staggered array of opposite signed vortices distributing along the centerline. Thus, a '2P + 2S' wake structure is generated. Meanwhile, in Fig. 12(b2), instead of moving transversely, the formed vortex pair rolls along the side edge of the hindmost foil. When B_1 arrives at the trailing edge of the foil in Fig. 12(b3), the foil tip is almost at its topmost position. In Fig. 12(b4), when the hindmost foil is pitching down, B_1 is stalled at the hindmost foil trailing edge and an opposite-signed vortex starts to come into being at the foil tip. At the same time, A₂ keeps moving downstream and distorts into a stretching trail. In Fig. 12(b1-b3), the stalled B_1 pairs with the newly generated trailing edge vortex and forms a vortex pair moving downstream, which is denoted by B'_1 and B_2 , and A_2 dissipates quickly into the downstream, which makes it hardly to be observe in the flow field.

The result of the wake formation analysis shows that, for both cases, the branched high-momentum jets are mainly caused by the vortex pairs formed during each oscillation period. However, when $\varphi_{2-1}=300^\circ$, $\varphi_{3-2}=120^\circ$, the vortex pair contains the trailing edge vortex of the second foil and the leading-edge vortex of the hindmost foil, and when $\varphi_{2-1}=300^\circ$, $\varphi_{3-2}=320^\circ$, the vortex pair is comprised of the leading-edge vortex and trailing edge vortex of the

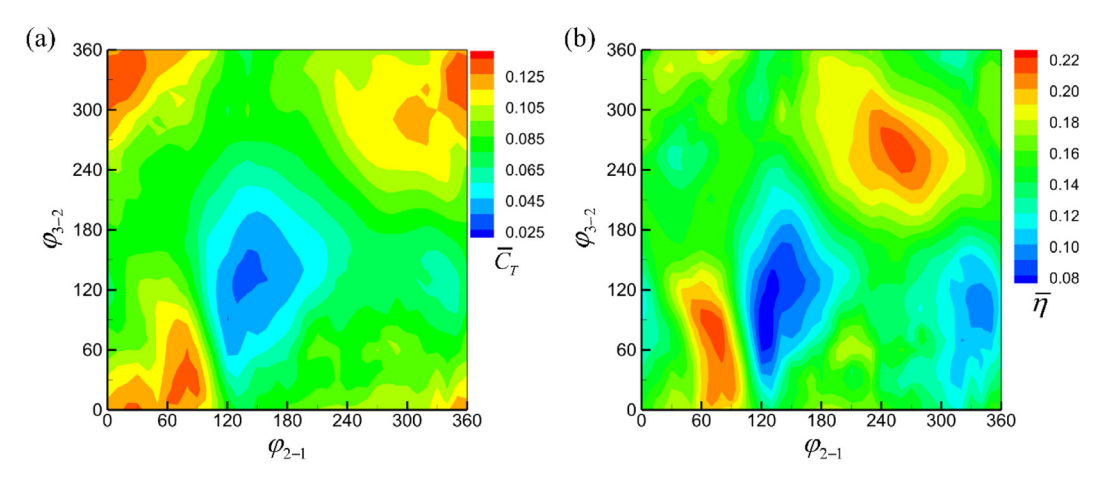


Fig. 13. Propulsive performance of the three tandem foil system at Re = 1000: (a) the collective thrust coefficient and (b) the collective propulsive efficiency.

hindmost foil. This explains why in Fig. 11(b2) and (b5), the branched high-momentum jets start from the leading edge of the hindmost foil and for the high-efficiency case, the branched jets start from the trailing edge of the hindmost foil.

With PIV experimental method, the '2P' wake structure was also observed behind the swimming eels (Müller et al., 2001) and zebrafish larvae (Müller et al., 2008). With one vortex from the body part and the other ipsilateral but opposite-signed vortex from the tail, one vortex pair is formed per half tail-beat. However, due to the complexity of the experimental measurements, the hydrodynamic benefits of this specific '2P' wake structure were not clearly identified. Though in Ref. Müller et al. (2001), three types of vortex interactions were proposed: the maximum thrust was attributed to a reverse von Kármán vortex street, the maximum efficiency was attributed to a von Kármán vortex street, and the high sideways force was attributed to the consecutively shedding ipsilateral body and tail vortices. In this work, we present that, with deliberately choosing the undulatory phase, the '2P' branched wake structure can achieve maximum thrust and efficiency simultaneously.

3.4. Effects of Reynolds number

To look into the effects of the Reynolds number, we examined the hydrodynamic performance of the tandem foil system at Re = 1000 and the results are shown in Fig. 13. Though, in general, Re = 500 and Re = 1000 share a similar trend, compared to Re = 500, the thrust and efficiency distributions of Re = 1000 cases are more complicated and there are a few differences need to be noted.

When Re = 500, the largest thrust and efficiency happen simultaneously at a single point ($\varphi_{2-1} = 300^\circ$, $\varphi_{3-2} = 320^\circ$), while when Re = 1000, the largest thrust and efficiency happen asynchronously at multiple points. For example, the maximum collective thrust happens at points ($\varphi_{2-1}=20^\circ$, $\varphi_{3-2}=340^\circ$) and ($\varphi_{2-1}=360^\circ$, $\varphi_{3-2}=330^\circ$), both of which show a thrust coefficient around 0.132 and the maximum collective efficiency happens at two points, $(\varphi_{2-1} = 260^\circ, \varphi_{3-2} = 260^\circ)$ and $(\varphi_{2-1} = 80^\circ, \varphi_{3-2} = 70^\circ)$, both of which show an efficiency around 21.5%. In Fig. 13, it is also noticed that, the two most efficient cases are still superior to most of the other cases in the collective thrust. In Fig. 14, the wake evolutions of these two cases are shown. Though a '2P' wake can still be observed in Fig. 14(a1, a2), the formation of this wake structure is slightly different from what we observed in case ($\varphi_{2-1} = 300^\circ$, $\varphi_{3-2} = 320^\circ$), Re = 500. Instead of pairing with the trailing edge vortex B_2 , the leading-edge vortex B_1 generated by the hindmost foil merges with it at about 0.75C away from the hindmost foil trailing edge, and then the merged vortex pairs with the trailing edge vortex A_2 of the second foil. The formed vortex pair moves downstream and shows a '2P' wake in the downstream. Fig. 14(b1, b2) shows the wake of case ($\varphi_{2-1} = 80^\circ$, $\varphi_{3-2} = 70^\circ$) for comparison. It is noticed that, different from case ($\varphi_{2-1}=260^\circ$, $\varphi_{3-2}=260^\circ$), in Fig. 14(b1), due to the effects of the vortex pair generated at the leading edge of the second foil, the trailing edge vortex A_2 of the second foil is compressed through the centerline and merges with the leading-edge vortex B_1 of the hindmost foil. A distinct vortex structure is formed and labeled as $A_2 + B_1$. Part of this vortex structure is shed into the downstream, following the likely-signed hindmost foil trailing edge vortex B_2 , as shown in Fig. 14(b2), and forms a narrow curved band behind it. The remaining part of $A_2 + B_1$ pairs with the opposite-signed trailing edge vortex, which is generated after B_2 , and moves downstream. However, due to the fast attenuation of this part, only a reverse von Kármán wake is observed in the downstream.

The results of the Reynolds number effect study show that, with the increase of the Reynolds number, though the maximum thrust and efficiency may not be achieved simultaneously, the '2P' wake structure can still achieve a performance superior to the reverse von Kármán vortex street in some cases. However, it is still worth mentioning that, in nature, many marine creatures experience a much higher Reynolds number than 1000 (Gazzola et al., 2014), thus, future

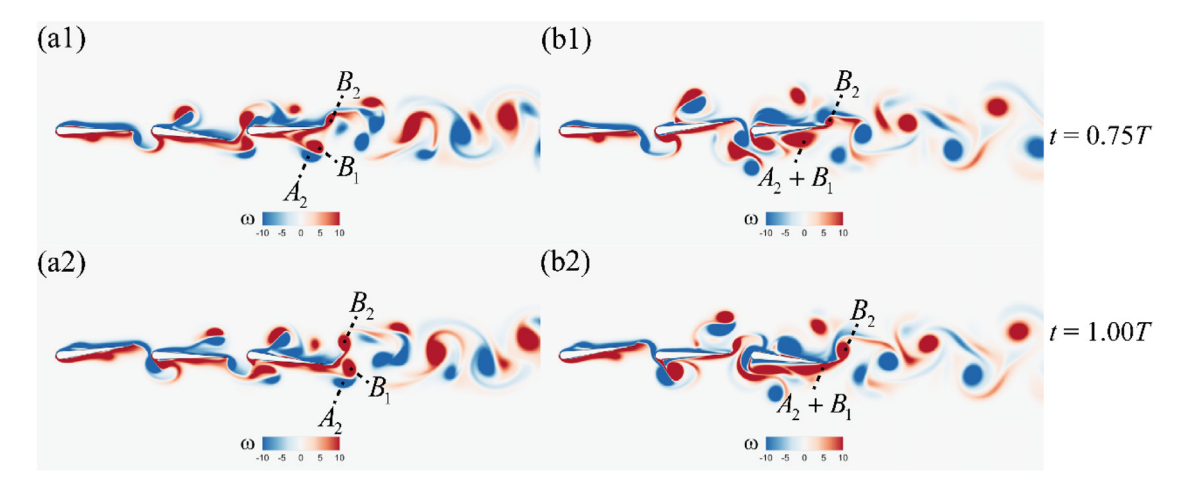


Fig. 14. Vortex structures of the high collective efficiency cases ($\varphi_{2-1}=260^\circ$, $\varphi_{3-2}=260^\circ$) (a1, a2) and ($\varphi_{2-1}=80^\circ$, $\varphi_{3-2}=70^\circ$) (b1, b2) at selected time instants t=0.75T (a1, b1) and t=1.00T (a2, b2).

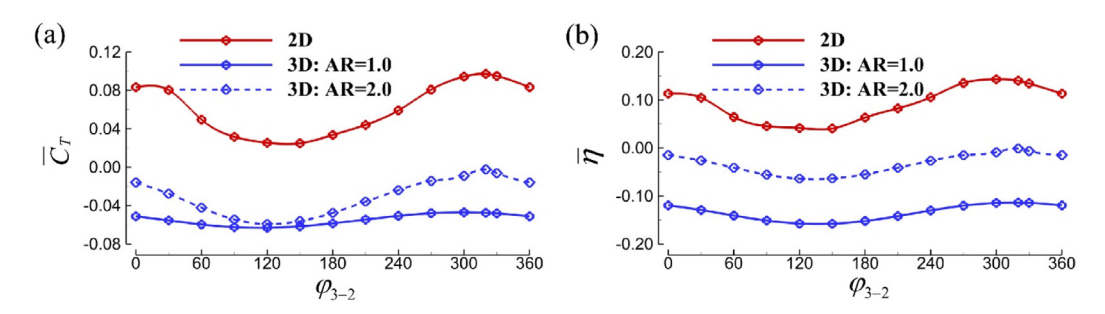


Fig. 15. Comparison of hydrodynamic performance between 2D and 3D three tandem foil system with $\varphi_{2-1} = 300^{\circ}$ and φ_{3-2} ranging from 0° to 360° . (a) Collective cycle-averaged thrust and (b) collective propulsive efficiency.

studies are still needed to interpret the intertwined relationship between the hydrodynamic performance and the wake structure at different Reynolds numbers.

3.5. Effects of three-dimensionality

In this section, the effects of three-dimensionality on the hydrodynamic performance and wake evolution of the three-foil system are investigated, including spanwise compression, transverse expansion and wake breakdown.

To explore the three-dimensionality effects, simulations are conducted using foils with different aspect ratios (AR = 1.0, 2.0). Similar to 2D cases, around the hydrofoils, a denser mesh region is deployed, with a resolution of 78, 190, 66 cells per chord length in the x, y and z directions. Fig. 15 compares the collective cycle-averaged thrust and collective propulsive efficiency of the 3D cases to the 2D cases with $\varphi_{2-1} = 300^{\circ}$ and φ_{3-2} ranging from 0° to 360° . For both 2D and 3D systems with different AR, the results share a broad trend. In Fig. 15(b), the worst case happens when $\varphi_{3-2} = 120^{\circ}$ and the optimal case happens when φ_{3-2} is around 320° . Fig. 15(a) shows that, with a finite AR, the 3D foil system generates negative thrust force in the current condition we studied (St = 0.25, Re = 500). This corresponds with the previous study (Buchholz and Smits, 2008), where smaller AR results in smaller thrust generation. When AR is increased from 1.0 to 2.0, the thrust of the propulsion system is increased (actually it shows as drag reduction in Fig. 15(a)). And it is predictable that, with further increase in AR, the thrust force of the 3D system will increase to a positive value, which is close to the 2D case.

In Fig. 16, due to the complexity of the flow field at the midspan, which is mainly caused by the wake breakdown, a slice cut is taken at the quarter-span location to show the cycle-averaged streamwise velocity fields of the worst and optimal cases. When AR = 1.0, both cases in Fig. 16(a1, a2) show a branched wake structure following the trailing edge of the hindmost foil while for the optimal case $\varphi_{3-2} = 320^{\circ}$ in Fig. 16(a2), the downstream jets are much stronger when compared to that of Fig. 16(a1). In Fig. 16(b1, b2), due to the increase of the AR, the jet mode shares some similarities with the 2D cases. When $\varphi_{3-2} = 120^{\circ}$, a lower streamwise velocity region is observed in the downstream, which is similar to

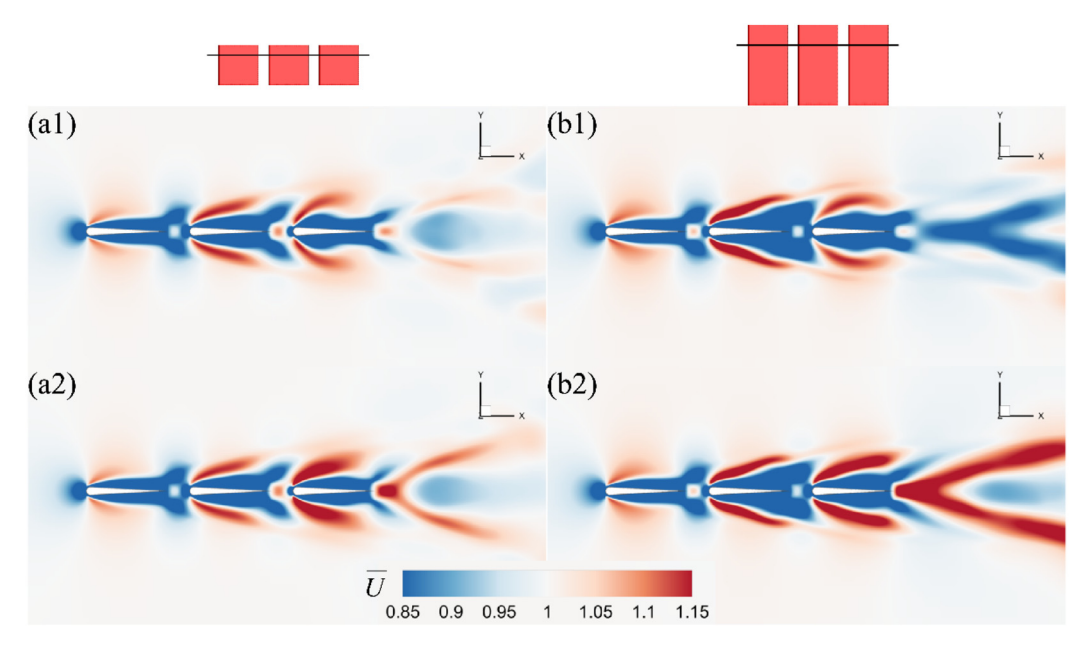


Fig. 16. Comparison of cycle-averaged streamwise velocity fields for three tandem foil system with different aspect ratios and phase differentials: (a1) AR = 1.0, $\varphi_{2-1} = 300^\circ$, $\varphi_{3-2} = 120^\circ$; (a2) AR = 1.0, $\varphi_{2-1} = 300^\circ$, $\varphi_{3-2} = 320^\circ$; (b1) AR = 2.0, $\varphi_{2-1} = 300^\circ$, $\varphi_{3-2} = 120^\circ$; and (b2) AR = 2.0, $\varphi_{2-1} = 300^\circ$, $\varphi_{3-2} = 320^\circ$. The slice cuts are taken at quarter-span location.

what happens in Fig. 11(b2), though in Fig. 16(b1), the low streamwise velocity region splits into a branched structure later. When $\varphi_{3-2} = 320^\circ$, similar to Fig. 11(b5), in the downstream, a significant pair of high momentum jets is observed. Fig. 17 shows the z-vorticity contours of the 3D worst and optimal cases with AR = 2.0. From Fig. 17, the first thing we notice is that, the vortex shedding from the second foil can still induce a stronger hindmost foil leading-edge vortex. And then, when the formed vortex pair $(A_2 \text{ and } B_1)$ moves downstream, a hindmost foil trailing edge vortex (B_2) comes into being. Due to the pitching motion of the foil, in Fig. 17(a2), the likely-signed B_1 and B_2 , they merge with each other at the trailing edge of the foil and then move downstream together, while A_2 dissipates immediately. Later, in the wake, the merged vortex is observed to separate into two, again. This explains why in Fig. 16(b1), a coherent low momentum region shows first and then splits into a branched structure. In contrast, in Fig. 17(b2), the vortex B_1 from the leading-edge vortex pair pairs with the opposite signed trailing edge vortex B_2 and forms a new vortex pair transferring downstream. One thing we need to note here is that, in this case, the vortex B_1 is too feeble to last long. Though in the wake, a distorted '2P' structure can still be observed, the stretched trail structure, which is labeled as 'T' in Fig. 17(b2), is not from the leading edge of the hindmost foil, but the spanwise tips. To identify the vortex origins, the 3D vortex structures of these two cases are plotted in Fig. 18. Similar to what is observed from a pitching panel (Buchholz and Smits, 2008), horseshoe vortices are found in the downstream. The wake breakdown occurs about 1.0C away from the hindmost foil trailing edge, this is attributed to the presence of the streamwise vortices generated by the spanwise tips of the pitching foil (Green et al., 2011). However, some differences still need to be addressed between these two cases. Compared to the worst case in Fig. 18(a1, a2), the best case in Fig. 18(b1, b2) shows stronger vortices at the trailing edge and spanwise tips of the hindmost foil. From the lateral view (Fig. 18(a2, b2)), we notice that, the optimal case shows a greater spanwise compression, which is normally caused by the streamwise vortices generated by the spanwise tips and related to a larger Strouhal number (Green et al., 2011; King et al., 2018). However, in our current study, all the foils share the same pitching frequency and amplitude. The reasons for the larger spanwise compression are not clear yet. Future works need to be conducted to reveal the detailed vortex interactions in the 3D cases and explore the spanwise wake compression mechanism.

4. Conclusions

With high-fidelity numerical simulations, we present the effects of phase differences on the hydrodynamic performance and vortex wakes of the multiple tandem foil systems. The results of two tandem foils show good similarities with previous studies (Boschitsch et al., 2014; Kurt and Moored, 2018), where the phase difference has been proven to influence the collective performance of the propulsion systems. With the parameters considered in the present study, the collective efficiency of the two-foil system reaches to a peak value $\bar{\eta} = 6.5\%$, with a collective thrust of $\bar{C}_T = 0.044$, when the phase difference is $\varphi_{2-1} = 300^\circ$. In addition, in current two-foil system simulations, both the optimal and worst cases show a '2S' coherent far-field wake structure.

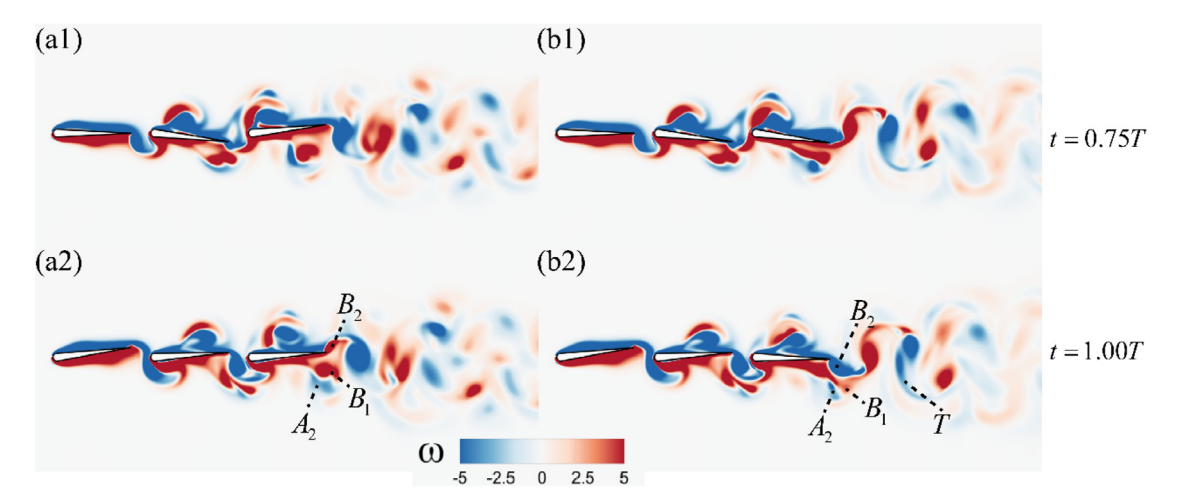


Fig. 17. Comparison of z-vorticity contours of three foil system with AR = 2.0 between the worst case (a1, a2) $\varphi_{2-1} = 300^{\circ}$, $\varphi_{3-2} = 120^{\circ}$ and the optimal case (b1, b2) $\varphi_{2-1} = 300^{\circ}$, $\varphi_{3-2} = 320^{\circ}$ at selected time instants t = 0.75T (a1, b1) and t = 1.00T (a2, b2). The slice cuts are taken at quarter-span location.

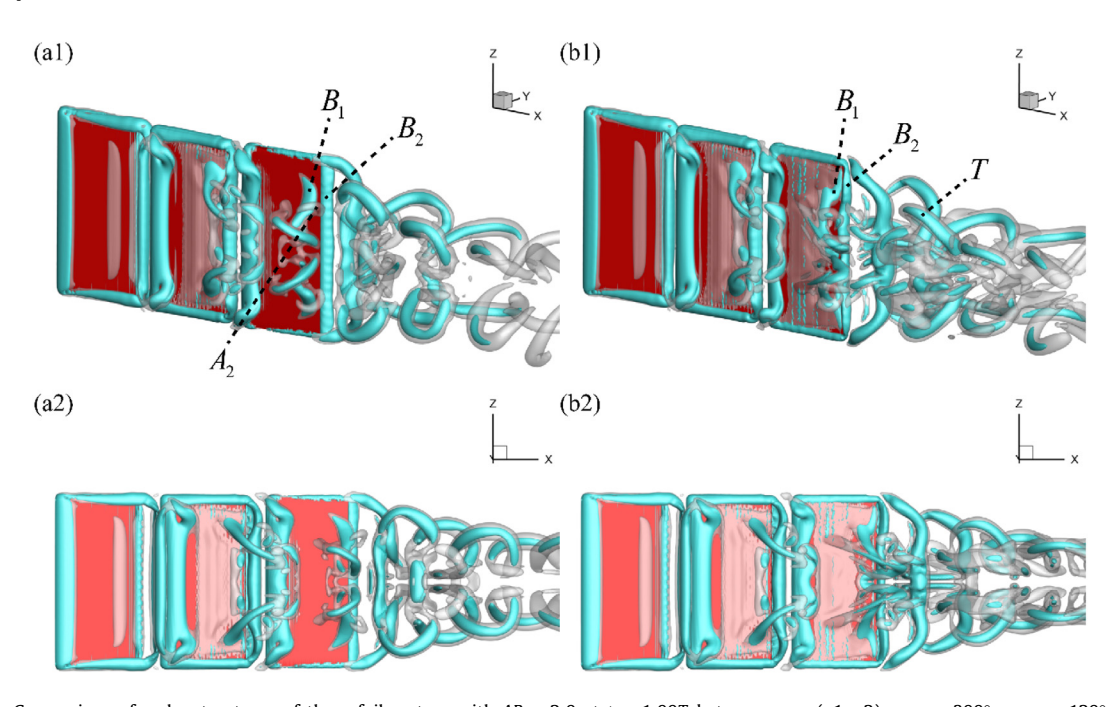


Fig. 18. Comparison of wake structures of three foil system with AR = 2.0 at t = 1.00T between case (a1, a2) $\varphi_{2-1} = 300^{\circ}$, $\varphi_{3-2} = 120^{\circ}$ and case (b1, b2) $\varphi_{2-1} = 300^{\circ}$, $\varphi_{3-2} = 320^{\circ}$. (a1, b1) shows the perspective view and (a2, b2) shows the lateral view. The wake structures are visualized by the iso-surface of Q-criterion. Q = 4.0 and Q = 15.0 are visualized in gray and cyan, respectively. The latter highlights the vortex core.

Beyond the two-foil system, the hydrodynamic performance and vortex dynamics of a three tandem foil system are studied. With the phase differences φ_{2-1} and φ_{3-2} ranging from 0° to 360°, in a phase diagram, the collective hydrodynamic performance and the corresponding vortex wakes are mapped out. Compared to the two-foil system, by introducing one more foil and tailoring the phase differences, the optimal three-foil system achieves an 118% increase in collective thrust and an 115% increase in collective efficiency. The '2P' wake structure is found to be responsible for the performance enhancement and each vortex pair contains one vortex from the hindmost foil leading edge and the other one from the hindmost foil trailing edge. Corresponding to this, a branched wake mode is observed in the downstream. Our results show that, the efficient propulsion is not essentially related to a coherent wake mode. The high thrust and efficiency '2P' wake structure may be used to explain the propulsion mechanisms of some fishes, which have been found to generate '2P' wakes in the downstream (Müller et al., 2001, 2008).

The effects of Reynolds number are also studied by comparing the hydrodynamic performance of the three-foil systems at Re=500 and Re=1000. The results show that when increasing the Reynolds number from 500 to 1000, the largest collective thrust and efficiency are reached asynchronously at multiple points. Though when Re=1000, the maximum collective efficiency happens at two points, $(\varphi_{2-1}=260^\circ,\varphi_{3-2}=260^\circ)$ and $(\varphi_{2-1}=80^\circ,\varphi_{3-2}=70^\circ)$, the '2P' wake pattern can still be observed in the downstream for the most efficient cases, which is similar to the lower Reynolds number cases. In addition, the analysis of hydrodynamic performance of finite-aspect-ratio pitching foils shows that, with $\varphi_{2-1}=300^\circ$, when increasing φ_{3-2} from 0° to 360° , the 3D three-foil system has a similar trend in thrust generation and propulsive efficiency as 2D foil systems, with lower magnitudes. The simulations show that the wake of high-performance finite-aspect-ratio pitching foils is dominated by two sets of interconnected vortex loops. For finite-aspect-ratios, these vortex loops evolve into a compressed vortex structure as they move downstream. The motion of these vortex structures leads to the formation of twin oblique jets which are most clearly visible in the time-averaged wake profiles for these finite-aspect-ratio cases.

Declaration of competing interest

The authors declare that they have no known competing financial interests or personal relationships that could have appeared to influence the work reported in this paper.

Data availability

The data that support the findings of this study are available within the article.

Acknowledgments

This is work is supported by ONR-MURI Grant N00014-14-1-0533 and NSF, United States CNS-1931929.

References

Akhtar, I., Mittal, R., Lauder, G.V., Drucker, E., 2007. Hydrodynamics of a biologically inspired tandem flapping foil configuration. Theor. Comput. Fluid Dyn. 21, 155–170.

Boschitsch, B.M., Dewey, P.A., Smits, A.J., 2014. Propulsive performance of unsteady tandem hydrofoils in an in-line configuration. Phys. Fluids 26, 051901.

Broering, T.M., Lian, Y.-S., 2012. The effect of phase angle and wing spacing on tandem flapping wings. Acta Mech. Sinica 28, 1557-1571.

Buchholz, J.H., Smits, A.J., 2008. The wake structure and thrust performance of a rigid low-aspect-ratio pitching panel. J. Fluid Mech. 603, 331–365. Drucker, E.G., Lauder, G.V., 2001. Locomotor function of the dorsal fin in teleost fishes: experimental analysis of wake forces in sunfish. J. Exp. Biol. 204, 2943–2958.

Drucker, E.G., Lauder, G.V., 2005. Locomotor function of the dorsal fin in rainbow trout: kinematic patterns and hydrodynamic forces. J. Exp. Biol. 208, 4479–4494.

Gazzola, M., Argentina, M., Mahadevan, L., 2014. Scaling macroscopic aquatic locomotion. Nat. Phys. 10, 758.

Green, M.A., Rowley, C.W., Smits, A.J., 2011. The unsteady three-dimensional wake produced by a trapezoidal pitching panel. J. Fluid Mech. 685, 117–145.

Han, P., Lauder, G.V., Dong, H., 2020. Hydrodynamics of median-fin interactions in fish-like locomotion: Effects of fin shape and movement. Phys. Fluids 32, 011902.

Khalid, M.S.U., Wang, J., Akhtar, I., Dong, H., Liu, M., Hemmati, A., 2021. Why do anguilliform swimmers perform undulation with wavelengths shorter than their bodylengths? Phys. Fluids 33, 031911.

King, J.T., Kumar, R., Green, M.A., 2018. Experimental observations of the three-dimensional wake structures and dynamics generated by a rigid, bioinspired pitching panel. Phys. Rev. Fluids 3, 034701.

Kurt, M., Moored, K.W., 2018. Flow interactions of two-and three-dimensional networked bio-inspired control elements in an in-line arrangement. Bioinspiration Biomim. 13, 045002.

Lewin, G.C., Haj-Hariri, H., 2003. Modelling thrust generation of a two-dimensional heaving airfoil in a viscous flow. J. Fluid Mech. 492, 339-362.

Li, C., Dong, H., 2016. Three-dimensional wake topology and propulsive performance of low-aspect-ratio pitching-rolling plates. Phys. Fluids 28, 071901.

Liu, G., Ren, Y., Dong, H., Akanyeti, O., Liao, J.C., Lauder, G.V., 2017. Computational analysis of vortex dynamics and performance enhancement due to body-fin and fin-fin interactions in fish-like locomotion. J. Fluid Mech. 829, 65–88, %@ 0022-1120.

Maia, A., Lauder, G.V., Wilga, C.D., 2017. Hydrodynamic function of dorsal fins in spiny dogfish and bamboo sharks during steady swimming. J. Exp. Biol. 220. 3967–3975.

Mittal, R., Dong, H., Bozkurttas, M., Najjar, F., Vargas, A., Loebbecke, A.Von., 2008. A versatile sharp interface immersed boundary method for incompressible flows with complex boundaries. J. Comput. Phys. 227, 4825–4852.

Müller, U.K., van den Boogaart, J.G., van Leeuwen, J.L., 2008. Flow patterns of larval fish: undulatory swimming in the intermediate flow regime. J. Exp. Biol. 211, 196–205.

Müller, U.K., Smit, J., Stamhuis, E.J., Videler, J.J., 2001. How the body contributes to the wake in undulatory fish swimming: flow fields of a swimming eel (Anguilla anguilla). J. Exp. Biol. 204, 2751–2762.

Pan, Y., Dong, H., 2020. Computational analysis of hydrodynamic interactions in a high-density fish school. Phys. Fluids 32, 121901.

Peng, Z.-R., Huang, H., Lu, X.-Y., 2018. Collective locomotion of two self-propelled flapping plates with different propulsive capacities. Phys. Fluids 30.

Standen, E.M., 2010. Muscle activity and hydrodynamic function of pelvic fins in trout (Oncorhynchus mykiss). J. Exp. Biol. 213, 831–841.

Standen, E., Lauder, G.V., 2007. Hydrodynamic function of dorsal and anal fins in brook trout (Salvelinus fontinalis). J. Exp. Biol. 210, 325-339.

Triantafyllou, G.S., Triantafyllou, M., Grosenbaugh, M., 1993. Optimal thrust development in oscillating foils with application to fish propulsion. J. Fluids Struct. 7, 205–224.

- Tytell, E.D., 2006. Median fin function in bluegill sunfish Lepomis macrochirus: streamwise vortex structure during steady swimming. J. Exp. Biol. 209, 1516–1534.
- Van Buren, T., Floryan, D., Bode-Oke, A.T., Han, P., Dong, H., Smits, A., 2019. Foil shapes for efficient fish-like propulsion. In: AIAA Scitech 2019 Forum. p. 1379.
- Van Kan, J., 1986. A second-order accurate pressure-correction scheme for viscous incompressible flow. SIAM J. Sci. Stat. Comput. 7, 870-891.
- Wang, J., Wainwright, D.K., Lindengren, R.E., Lauder, G.V., Dong, H., 2020. Tuna locomotion: a computational hydrodynamic analysis of finlet function. J. R. Soc. Interface 17, 20190590.
- Williamson, C.H., Roshko, A., 1988. Vortex formation in the wake of an oscillating cylinder. J. Fluids Struct. 2, 355-381.
- Xu, G., Duan, W., Xu, W., 2017. The propulsion of two flapping foils with tandem configuration and vortex interactions. Phys. Fluids 29, 097102.
- Yuan, C., Liu, G., Ren, Y., Dong, H., 2015. Propulsive performance and vortex interactions of multiple tandem foils pitching in line. In: 45th AlAA Fluid Dynamics Conference. p. 3220.
- Zhong, Q., Dong, H., Quinn, D.B., 2019. How dorsal fin sharpness affects swimming speed and economy. J. Fluid Mech. 878, 370-385.